Ultrastrong plasmon-phonon coupling via epsilon-near-zero nanocavities

Daehan Yoo[1,+]**, Fernando de León-Pérez**[2,3,+]**, Matthew Pelton**[4]**,**
In-Ho Lee[1]**, Daniel A. Mohr**[1]**, Markus B. Raschke**[5]**,**
Joshua D. Caldwell[6]**, Luis Martín-Moreno**[3,*]**, and Sang-Hyun Oh**[1,*]

[1]Department of Electrical and Computer Engineering, University of Minnesota, 200 Union St. S.E., Minneapolis, MN, USA
[2]Centro Universitario de la Defensa de Zaragoza, Ctra. de Huesca s/n, E-50090 Zaragoza, Spain
[3]Instituto de Ciencia de Materiales de Aragón and Departamento de Física de la Materia Condensada, CSIC-Universidad de Zaragoza, E-50009 Zaragoza, Spain
[4]Department of Physics, University of Maryland, Baltimore County, Baltimore, MD, USA
[5]Department of Physics and JILA, Department of Chemistry, University of Colorado, Boulder, CO, USA
[6]Department of Mechanical Engineering, Vanderbilt University, Nashville, TN, USA
[*]E-mail: lmm@unizar.es and sang@umn.edu
[+]these authors contributed equally to this work

ABSTRACT

Vibrational ultrastrong coupling (USC), where the light-matter coupling strength is comparable to the vibrational frequency of molecules, presents new opportunities to probe the interactions of molecules with zero-point fluctuations, harness cavity-enhanced chemical reactions, and develop novel devices in the mid-infrared regime. Here we use epsilon-near-zero nanocavities filled with a model polar medium (SiO_2) to demonstrate USC between phonons and gap plasmons. We present classical and quantum mechanical models to quantitatively describe the observed plasmon-phonon USC phenomena and demonstrate a modal splitting of up to 50% of the resonant frequency (normalized coupling strength $\eta > 0.25$). Our wafer-scale nanocavity platform will enable a broad range of vibrational transitions to be harnessed for USC applications.

Introduction

Traditionally, two regimes of light-matter interactions have been considered: weak coupling (WC), when losses exceed the light-matter coupling strength, and strong coupling (SC), when the coupling strength dominates[1,2]. For weak-coupling phenomena such as the Purcell effect[3], Fano interference[4], and surface-enhanced infrared absorption[5], the coupled systems exchange energy on a time scale slower than the decay rates. In contrast, within the SC regime, the oscillators exchange their energy reversibly and coherently over an extended time frame that is longer than the decay rates[6–14] – a prerequisite for quantum information processing[15]. Furthermore, strongly-coupled hybridized modes exhibit distinct energy levels and characteristics modified from those of the bare constituents, leading to novel phenomena such as the modification of chemical reaction rates[2,16,17] and ground-state reactivity[18].

When the normalized coupling strength, η (defined as the ratio of the light-matter coupling strength, g, to the mid-gap frequency, ω, which is roughly half the mode splitting divided by ω), of the system exceeds ~ 0.1, even more exotic phenomena can occur. In this ultrastrong coupling (USC) regime[1,2,19,20], some of the standard approximations that are valid for WC and SC, such as the rotating-wave approximation, are expected to break down. Furthermore, transitioning from SC to USC implies that the hybrid mode exhibits substantially more oscillations between light and matter states prior to decay, and such fast and efficient interactions can enable novel ultrafast devices[19,21]. Another striking phenomenon predicted in the USC regime, resulting from the antiresonant term in the light-matter coupling equation, is the possibility to extract virtual photons from the modified ground state via a dynamic Casimir effect[22,23] Also, USC between light and molecules can modify or enhance chemical reactions beyond what is possible in the SC regime[19].

USC has been demonstrated using photochromic molecules[24], circuit QED systems[25], intersubband polaritons[26], molecular liquids[27], and 2D electron gases[28]. SC to vibrational modes at mid-infrared (MIR) frequencies has been demonstrated in various systems[18,29–32], enabling applications such as surface-enhanced vibrational spectroscopy[5,33], thermal emission and signature control, and modified heat transfer. It has been challenging, however, to achieve USC at MIR frequencies, particularly in solid-state systems, because of the relatively weak oscillator strengths for vibrational modes originating from lattice ionic

motions. Previous demonstrations have involved extended microcavity structures[2, 18, 27], opening up a new physical regime at these technologically important frequencies, but with limited possibilities for novel nonlinear effects.

Here we demonstrate vibrational USC within nanocavities, drastically reducing the size of the system and thus the amount of material involved in achieving MIR USC. Specifically, we use coaxial nanocavities, which exhibit strong transmission resonances and field enhancements close to the cutoff frequency of the TE_{11}-like mode; these can be understood as resulting from excitation of the zeroth-order Fabry-Perot resonance[34] or alternatively, as arising from the effective epsilon-near-zero (ENZ) effect[35–37]. We couple this nano-coax ENZ mode to the lattice vibrations of SiO_2 and demonstrate MIR USC with a mode splitting exceeding 50% of the vibrational transition frequency ($\eta > 0.25$) within a solid-state system.
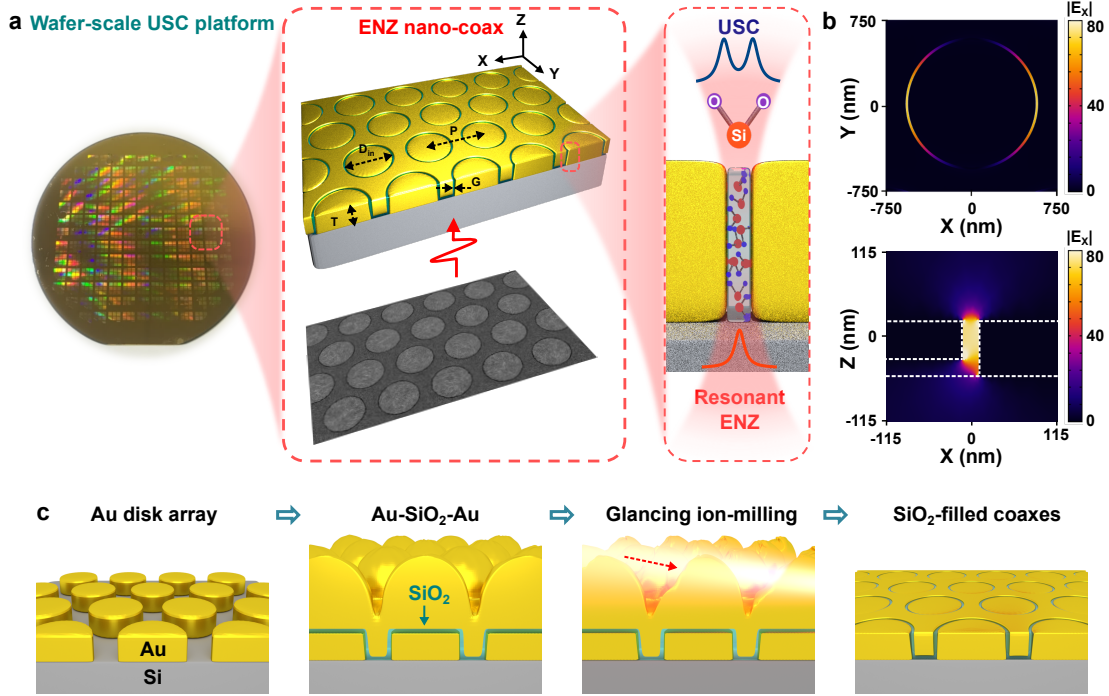

Figure 1. Wafer-scale resonant ENZ nanocavity platform for USC. (a) Geometrical parameters and illustration of SiO_2 phonons interacting with the ENZ mode of the nanocavity. (inset) Scanning electron micrograph (SEM) of coaxial nanocavities with 21 nm gap, 790 nm diameter, 1190 nm period, and 80 nm Au thickness. (b) Computed E_x field profiles of a coaxial nanocavity (D=1120 nm and G=21 nm) showing a lateral section (upper) and a vertical section (lower) of the ENZ transmission resonance. (c) Process flow based on atomic layer deposition and wafer-scale glancing-angle ion milling.

Results

In our USC platform, SiO_2-filled coaxial nanoapertures fabricated into a metal (Au) film are hexagonally arranged with varied gap size (G), diameter (D), and lattice periodicity (P) (Fig. 1a). Unlike conventional approaches of selectively etching annular gaps in metal films, we adopt a novel fabrication approach called atomic layer lithography[36] to create dielectric-filled nanogaps in metal films (Fig. 1c and Method section). After employing standard photolithography to define gold disk arrays on a silicon wafer, SiO_2 films are conformally grown via atomic layer deposition (ALD) on the exposed surfaces and sidewalls, followed by subsequent metal cladding layer deposition and planarization via glancing-angle ion milling. This batch process can produce wafer-sized arrays of coaxial apertures with gap size down to 1 nm, limited only by the ALD growth. For very narrow gaps, TE_{11} coaxial modes have a strong plasmonic character. Such modes are characterized by an effective dielectric constant that is approximately zero at cutoff. This resonance can be shifted toward longer wavelengths without sacrificing modal confinement by increasing the coax diameter without changing the gap width. In addition, the associated spatially uniform optical field (Fig. 1b lower panel) that results from the very long wavelength associated with near-zero-permittivity provides efficient coupling to the material and its resonances within the deeply sub-diffractional gaps. We also note that the ENZ resonance is a single-aperture effect, thus, the existence of an array is not required for the transmission resonance we utilize (Sec. S2). Further, we note that the resonant optical properties of our wafer-scale coaxial ENZ system are robust against process variations and inhomogeneous broadening for two reasons: First, the critical dimension, i.e. the width of the nanogap,

is lithography-independent and precisely defined by the thickness of the SiO$_2$ film grown by ALD. Second, the ENZ mode (i.e., the zeroth-order Fabry-Perot resonance) is independent of the cavity length; thus, the thickness variation of the gold film does not lead to noticeable inhomogeneous broadening.

Our coaxial nanocavities were designed to spectroscopically sweep the bare ENZ resonance across the Reststrahlen band of SiO$_2$, which is defined by the transverse optical (TO) and longitudinal optical (LO) phonons of SiO$_2$ (Fig. 2a). Transmission spectra through the nanocavity arrays were measured by far-field Fourier transform infrared (FTIR) spectroscopy over a large-area (5 mm × 5 mm) chip containing arrays of coaxial nanocavities, with diameters ranging from 430 nm to 1120 nm in 30 nm steps. The normalized transmission spectra for coaxial nanocavities filled with 21 nm-thick SiO$_2$ are plotted in Fig. 2b. The observed transmission features a clear anticrossing behavior characteristic of SC. Coaxial nanocavities at the ENZ condition show extraordinary optical transmission (EOT)[38], since incident light with wavelengths 5-13 μm can pass through the annular gaps that are over thousand times narrower than the wavelength, with the measured absolute transmittance as high as 60%.
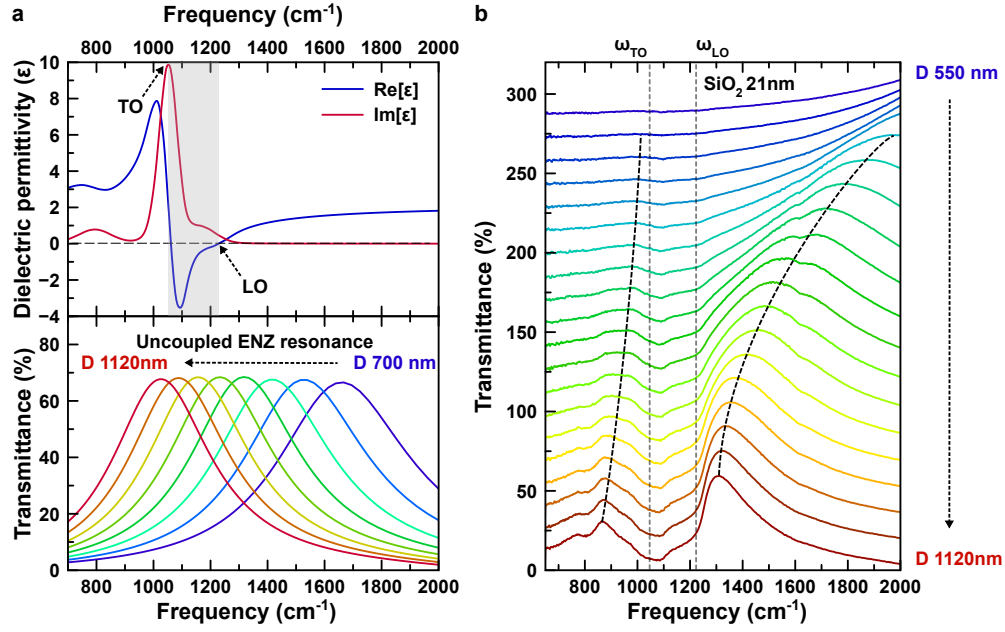
Figure 2. Normal mode splittings due to ultrastrong phonon-plasmon coupling. (a) Dielectric function[39] of SiO$_2$ (top) and ENZ transmission resonances (bottom) of the coaxial nanoapertures ($G = 21$ nm, diameter from 700 nm to 1120 nm), simulated with a frequency-independent dielectric constant ε_∞ inside the aperture. This calculation shows that the bare cavity resonance sweeps through the entire Reststrahlen band for the considered diameters (Sec. S1). (b) Normalized experimental transmission spectra of SiO$_2$-filled coaxial Au nanocavities, for G=21 nm and $D = 550$ to 1120 nm. Black dashed guide lines indicate the lower and upper polariton branches.

Although these results suggest that the SiO$_2$ phonons and cavity photons are strongly coupling, the split transmission peaks could alternatively be interpreted as the result of a single broad transmission resonance being quenched in a central frequency range by the strong vibrational absorption close to ω_{TO}. To clarify the origin of the split transmission peaks, we perform a theoretical analysis of the coupled system to be compared to our experimental results.

Electromagnetic propagation in waveguides is usually based on a description where the phononic degrees of freedom have been integrated out, providing an effective medium $\varepsilon(\omega)$ for the propagation of the photon (Sec. S3). However, in order to determine whether the system is in the SC regime, it is essential to retain both phononic and photonic degrees of freedom. We therefore consider a given waveguide mode M, characterized by a wavevector k along the waveguide axes (in this case, M=TE$_{11}$, the fundamental mode of the coaxial waveguide). When the aperture is filled with a uniform dielectric constant ε_∞ (originating from coupling to electronic degrees of freedom), the electric field, $\mathbf{E} = E\mathbf{E}_M$, satisfies the wave equation

$$\nabla \times \nabla \times E\mathbf{E}_M - \varepsilon_\infty \frac{\omega_k^2}{c^2} E\mathbf{E}_M = 0, \tag{1}$$

where E is the field amplitude and $\mathbf{E}_M$ is a normalized transverse solution of Maxwell equations (Sec. S4). When the phononic

material fills the waveguide, we assume a local relation (valid for non-dispersive vibrational modes) between $\mathbf{E}$ and the relative displacement of ions, $\mathbf{x}$, following[40]. Then, for a given mode profile, $\mathbf{E}(\mathbf{r}) = E\,\mathbf{E}_M(\mathbf{r},k)$ and $\mathbf{x}(\mathbf{r}) = x\,\mathbf{E}_M(\mathbf{r},k)$, with

$$\ddot{x} = \gamma_{11}x + \gamma_{12}E, \tag{2}$$

$$P = \gamma_{12}x + \gamma_{22}E, \tag{3}$$

where P is the amplitude of polarization vector $\mathbf{P} = P\,\mathbf{E}_M$, $\gamma_{12}^2 = \omega_p^2 \varepsilon_\infty/4\pi$ is the coupling constant, $\omega_p^2 = \omega_{LO}^2 - \omega_{TO}^2$, $\gamma_{11} = -\omega_{TO}^2$, and $\gamma_{22} = (\varepsilon_\infty - 1)/4\pi$ (see Sec. S3). Note that γ_{22} incorporates the effect of the electronic resonances excited at higher frequencies. The wave equation becomes, in this case,

$$\nabla \times \nabla \times E\mathbf{E}_M - \frac{\omega^2}{c^2}(E + 4\pi P)\,\mathbf{E}_M = 0. \tag{4}$$

By inspection, we find that $\mathbf{E}_M(\mathbf{r},k)$ satisfies Eq. (4) if $\omega^2(E + 4\pi P) = \omega_k^2 E$ (strictly speaking, we are neglecting the variation between ω and ω_k in the impedance of the metal surrounding the waveguide; for a deeper analysis of how this affects the cutoff condition, see Secs. S2 and S5). This condition, together with Eqs. (2) and (3) can be expressed in a matrix form, stating that $\mathbf{E}_M(\mathbf{r},k)$ is still a solution of Maxwell equations but at a frequency ω satisfying

$$\begin{pmatrix} \omega^2 - \omega_{TO}^2 & \omega\,\omega_p \\ \omega\,\omega_p & \omega^2 - \omega_k^2 \end{pmatrix} \cdot \begin{pmatrix} \omega\,x \\ \sqrt{\varepsilon_\infty/4\pi}E \end{pmatrix} = 0. \tag{5}$$

(See Sec. S6 for a detailed derivation and a discussion of the effects of losses) Note that the simpler coupled harmonic oscillator model that is customarily used for fitting experimental data (see Sec. S7) does not show the ω-dependence of the off-diagonal terms and therefore cannot describe the polaritonic branches correctly (cf. Figs. 3a and S6).

We have used a classical approach here. For future work, especially the investigation of nonlinear optical effects, a full quantum mechanical description will be required, wherein off-resonant terms may be important and the rotating-wave approximation cannot necessarily be applied[41–45]. We therefore applied the canonical procedure of second quantization to the classical Hamiltonian (see Sec. S9 for details). For the sake of convenience, absorption was neglected and the geometry of the system was simplified to a coaxial resonator with perfect-electric-conductor walls. We obtain a Hopfield-like Hamiltonian[41] for interacting photons and phonons: $H = H_{photon} + H_{phonon} + H_{int}$, with

$$H_{photon} = \sum_m \hbar\omega_m \left(a_m^+ a_m + \frac{1}{2} \right), \tag{6}$$

$$H_{phonon} = \sum_m \hbar\omega_{TO} \left(b_m^+ b_m + \frac{1}{2} \right), \tag{7}$$

$$H_{int} = \sum_m \hbar \left[iC_m \left(a_m^+ b_m - a_m b_m^+ \right) + D_m \left(2a_k^+ a_m + 1 \right) \right. \tag{8}$$

$$\left. + iC_m \left(a_m b_m - a_m^+ b_m^+ \right) + D_m \left(a_m a_m + a_m^+ a_m^+ \right) \right]. \tag{9}$$

where a^+ (a) and b^+ (b) are the creation (annihilation) operators for photons and phonons, respectively, the sum is over modes m, and

$$C_m = \frac{\omega_p}{2}\sqrt{\frac{\omega_{TO}}{\omega_m}}, \quad D_m = \frac{\omega_p^2}{4\omega_m}. \tag{10}$$

As expected, given that the system comprises two coupled harmonic oscillators, diagonalizing the full Hamiltonian gives eigenfrequencies identical to those obtained from Eq. 5 (if absorption is neglected). In other words, the classical approach can be used to compute the polaritonic branches exactly when the system enters into the USC regime. The same behavior is valid for an arbitrary number of vibrational modes in the polar material (see Sec. S8, S10).

The outcome from Eq. 5 is thus one of the central results of our work. It shows that the dynamics between the vibrations and the plasmonic field in nanocavities are controlled by a 2×2 matrix similar to that used to discuss the coupled harmonic oscillator. The main difference is that the off-diagonal elements in Eq. 5 acquire a linear dependence on frequency (See Sec. S6). This does not have a large effect when analyzing anti-crossings, which focus on a narrow frequency range, but it is essential to understand the presence of an energy gap in the spectrum i.e., the fact that the low-frequency asymptote of the upper polariton and the high-frequency asymptote of the lower polariton do not coincide (see Fig. 3a).

We can therefore analyze the dependence of the ENZ resonant frequencies on the coax inner diameter using Eq. 5 (Fig. 3 c-f). As ω_p is independent of the hole shape and size, in this SC condition the ENZ resonances only depend on the bare ENZ frequency, $\omega_{ENZ}(D)$, which is obtained from the upper polariton branch (see Sec. S12). The model provides the estimate for
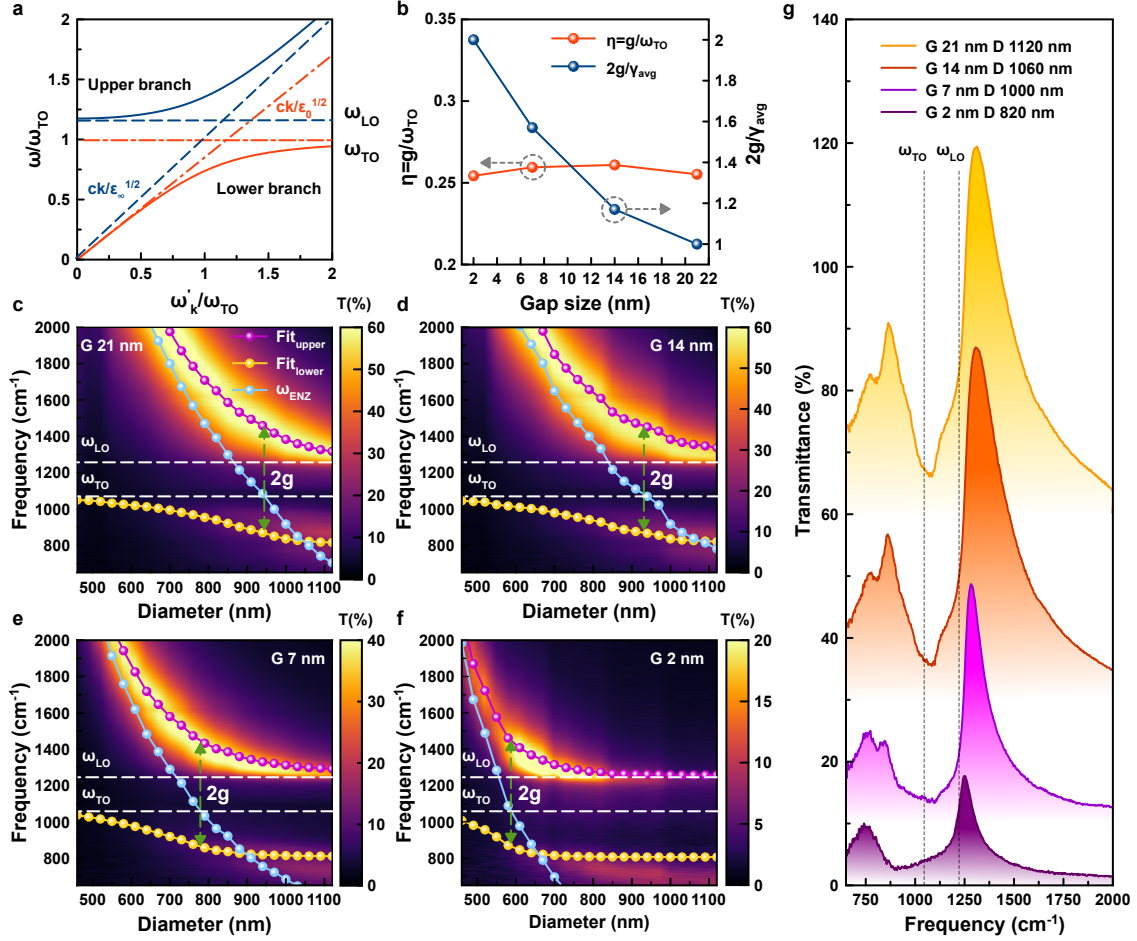
Figure 3. Dispersion mapping and validation of theoretical model. (a) The dispersion relation of bulk phonon polaritons supported in SiO_2 as calculated by Eq. 5 under the assumption that a single vibrational mode is excited. (b) The measured η and normalized mode splitting ($2g/\gamma_{avg}$) as a function of gap size are provided. (c-f) Dispersion maps of experimentally measured transmission spectra from coaxial apertures filled with SiO_2 with film thicknesses of (c) 21 nm, (d) 14 nm, (e) 7 nm, and (f) 2 nm. Analytical fitting of polaritonic resonances using Eq. (S14) (purple (upper) and yellow (lower) circle dots with a solid line). ω_{ENZ} (blue circles with a solid line) is used as a fitting parameter and indicates the resonance of the ENZ mode uncoupled from the polar phonons of SiO_2. The coupling strength, g is measured at the intersection between the uncoupled ENZ resonance and ω_{TO} (when the detuning is zero). (g) Transmission spectra measured when the bare ENZ mode crosses through the Reststrahlen band, showing distinct modal splitting and sharp resonant peaks (60% transmittance for the 21 nm-gap coax). Curves are shifted along the vertical axis for clarity.

the lower polariton branch as well. This procedure was followed because the lower polariton is more affected by additional vibrational resonances that have not been considered in this simple analysis.

For each gap size, we estimate g of the ENZ mode as half the frequency difference between upper and lower polariton branches when $\omega_{ENZ}(D) = \omega_{TO}$, with the results summarized in Table 1. Since the SiO_2 layer is added to our coaxial nanocavity during the fabrication process, it is not trivial to experimentally measure the bare ENZ resonance (i.e. empty gap). Instead, we measured the linewidth of a bare ENZ resonance at a higher frequency, where it is uncoupled from the SiO_2 phonons. As shown in Table 1, all cavities exhibit modal splittings that are larger than the average of the linewidths of the bare cavity resonances and of the TO phonon ($2g/\gamma_{avg} > 1$), indicating that the system is in the SC regime.

Moreover, the normalized coupling strength $\eta = g/\omega_{TO} > 0.25$, regardless of gap width, indicating that the systems are also in the USC regime[19]. For a single dipole emitter in a cavity, $g \propto 1/\sqrt{V}$. However, in the collective coupling as in our system, $g \propto \sqrt{N/V}$, where N is the number of dipoles coherently couple to the cavity mode. Thus, g depends only on the

density of molecules, N/V, and is independent of the coaxial gap width (see Sec. S3).

SiO$_2$ gap width (nm)	2	7	14	21
Bare ENZ mode linewidth (FWHM) (cm^{-1})	453	619	844	990
Average of bare ENZ and TO phonon linewidths, γ_{avg} (cm^{-1})	265	348	481	534
Normal mode splitting, $2g$ (cm^{-1})	534	546	549	537
Normalized mode splitting, $2g/\gamma_{avg}$	2.02	1.57	1.14	1.01
Normalized coupling strength, $\eta = g/\omega_{TO}$	0.254	0.26	0.261	0.255

Table 1. Mode splitting and normalized coupling strength.

Conclusions

Here we have constructed wafer-scale resonant coaxial nanocavities and achieved η greater than 0.25, originating from the interaction of the ENZ mode with SiO$_2$ phonons in nanometric gaps. The large magnitude of the splitting we observe - wider than the Reststrahlen band - clearly shows that the coupling strength is truly within the USC regime, and is not the manifestation of absorption induced within the forbidden band. To further elucidate this point, we also presented a theoretical framework (both classical and quantum mechanical) to model USC phenomena in the presence of the Reststrahlen band, which can be applied to homogeneous materials, waveguides, and resonant cavities. Our ENZ nanocavity platform features ultratight confinement of long-wavelength radiation while exhibiting EOT (up to 60% absolute transmission).

The ENZ nanocavities can be filled with a wide range of vibrationally-active materials, thus enabling USC to be realized using a broad range of materials in the MIR, far-IR, and terahertz spectral range. Furthermore, since single-nanometer-thick phononic films separate the core and cladding electrodes in each coax, the platform provides a route to combine electron tunneling with vibrational USC and EOT, which should enable observation of ground-state electroluminescence[46] and the dynamic Casimir effect[22, 23]. The ability to reach the USC regime in mass-produced ENZ cavities with ultrasmall gap volumes ($\approx \lambda^3/10^7$) can also open up new avenues to explore quantum nonlinear optical processes[47], multiphoton effects, higher-order nonlinear effects, and single-photon excitation of multiple atoms[48], which may lead to novel applications in quantum sensing, spectroscopy, optoelectronic devices, and frequency conversion[49].

Methods

Device fabrication

After pre-cleaning and pre-baking (200 °C for 3 min) steps, an undoped, double-side-polished 4-inch (100) Si wafer (University wafer) was spin-coated with AZ MIR701 photoresist for 45 s at 5,000 r.p.m., followed by baking at 90 °C for 90 s. The patterns of hexagonal hole arrays with 24 different diameters from 430 nm to 1120 nm were transferred onto the Si wafer by photolithography (Canon 2500 i3 stepper) with a dose of 150 mJ/cm^2, followed by post-exposure bake at 110 ° and development process with AZ 3000 MIF for 60 s. Hexagonal Au disk arrays were created on the Si wafer via directional evaporation of 3 nm Ti and 150 nm Au films (CHA, SEC 600), followed by a liftoff process with AZ kwik strip. After oxygen plasma cleaning (STS, 320PC) with 100 W for 30 s to remove photoresist residues, the Au disk arrays were coated conformally with a thin SiO$_2$ film using ALD (Cambridge Nano Tech Inc., Savannah) at a typical deposition rate of 1.2 Å/cycle, which was performed using ozone precursor and water vapor at 180 °C. After conformal sputtering of 3 nm Ti and 400 nm Au (AJA, ATC 2200), the top surface of 400 nm-thick Au-deposited disk patterns was planarized via glancing-angle ion milling using a 240 mA Ar$^+$ ion beam incident at 5 ° from the horizontal plane (Intlvac, Nanoquest) until the top entrance of coaxial nanocavities is exposed.

References

1. Törmä, P. & Barnes, W. L. Strong coupling between surface plasmon polaritons and emitters: a review. *Rep. Prog. Phys.* **78**, 013901, DOI: 10.1088/0034-4885/78/1/013901 (2015).

2. Ebbesen, T. W. Hybrid light-matter states in a molecular and material science perspective. *Acc. Chem. Res.* **49**, 2403–2412, DOI: 10.1021/acs.accounts.6b00295 (2016).

3. Pelton, M. Modified spontaneous emission in nanophotonic structures. *Nat. Photonics* **9**, 427–435, DOI: 10.1038/nphoton.2015.103 (2015).

4. Luk'yanchuk, B. *et al.* The fano resonance in plasmonic nanostructures and metamaterials. *Nat. Mater.* **9**, 707–715, DOI: 10.1038/nmat2810 (2010).

5. Neubrech, F. *et al.* Resonant plasmonic and vibrational coupling in a tailored nanoantenna for infrared detection. *Phys. Rev. Lett.* **101**, 157403, DOI: 10.1103/PhysRevLett.101.157403 (2008).

6. Yoshie, T. *et al.* Vacuum rabi splitting with a single quantum dot in a photonic crystal nanocavity. *Nature* **432**, 200–203, DOI: 10.1038/nature03119 (2004).

7. Reithmaier, J. P. *et al.* Strong coupling in a single quantum dot-semiconductor microcavity system. *Nature* **432**, 197–200, DOI: 10.1038/nature02969 (2004).

8. Aoki, T. *et al.* Observation of strong coupling between one atom and a monolithic microresonator. *Nature* **443**, 671–674, DOI: 10.1038/nature05147 (2006).

9. Liu, X. *et al.* Strong light–matter coupling in two-dimensional atomic crystals. *Nat. Photonics* **9**, 30–34, DOI: 10.1038/nphoton.2014.304 (2015).

10. Benz, F. *et al.* Single-molecule optomechanics in "picocavities". *Science* **354**, 726–729, DOI: 10.1126/science.aah5243 (2016).

11. Santhosh, K., Bitton, O., Chuntonov, L. & Haran, G. Vacuum rabi splitting in a plasmonic cavity at the single quantum emitter limit. *Nat. Commun.* **7**, 11823, DOI: 10.1038/ncomms11823 (2016).

12. Runnerstrom, E. L. *et al.* Polaritonic hybrid-epsilon-near-zero modes: Beating the plasmonic confinement vs propagation-length trade-off with doped cadmium oxide bilayers. *Nano Lett.* **19**, 948–957, DOI: 10.1021/acs.nanolett.8b04182 (2018).

13. Leng, H., Szychowski, B., Daniel, M.-C. & Pelton, M. Strong coupling and induced transparency at room temperature with single quantum dots and gap plasmons. *Nat. Commun.* **9**, 4012, DOI: 10.1038/s41467-018-06450-4 (2018).

14. Park, K.-D. *et al.* Tip-enhanced strong coupling spectroscopy, imaging, and control of a single quantum emitter. *Sci. Adv.* **5**, eaav5931, DOI: 10.1126/sciadv.aav5931 (2019).

15. Schoelkopf, R. J. & Girvin, S. M. Wiring up quantum systems. *Nature* **451**, 664–669, DOI: doi.org/10.1038/451664a (2008).

16. Dunkelberger, A., Spann, B., Fears, K., Simpkins, B. & Owrutsky, J. Modified relaxation dynamics and coherent energy exchange in coupled vibration-cavity polaritons. *Nat. Commun.* **7**, 13504, DOI: 10.1038/ncomms13504 (2016).

17. Munkhbat, B., Wersäll, M., Baranov, D. G., Antosiewicz, T. J. & Shegai, T. Suppression of photo-oxidation of organic chromophores by strong coupling to plasmonic nanoantennas. *Sci. Adv.* **4**, eaas9552, DOI: 10.1126/sciadv.aas9552 (2018).

18. Thomas, A. *et al.* Tilting a ground-state reactivity landscape by vibrational strong coupling. *Science* **363**, 615–619, DOI: 10.1126/science.aau7742 (2019).

19. Kockum, A. F., Miranowicz, A., Liberato, S. D., Savasta, S. & Nori, F. Ultrastrong coupling between light and matter. *Nat. Rev. Phys.* **1**, 19–40, DOI: 10.1038/s42254-018-0006-2 (2019).

20. Forn-Díaz, P., Lamata, L., Rico, E., Kono, J. & Solano, E. Ultrastrong coupling regimes of light-matter interaction. *Rev. Mod. Phys.* **91**, 025005, DOI: 10.1103/RevModPhys.91.025005 (2019).

21. Romero, G., Ballester, D., Wang, Y. M., Scarani, V. & Solano, E. Ultrafast quantum gates in circuit qed. *Phys. Rev. Lett.* **108**, 120501, DOI: 10.1103/PhysRevLett.108.120501 (2012).

22. Johansson, J. R., Johansson, G., Wilson, C. M. & Nori, F. Dynamical casimir effect in a superconducting coplanar waveguide. *Phys. Rev. Lett.* **103**, 147003, DOI: 10.1103/PhysRevLett.103.147003 (2009).

23. Wilson, C. M. *et al.* Observation of the dynamical casimir effect in a superconducting circuit. *Nature* **479**, 376–379, DOI: 10.1038/nature10561 (2011).

24. Schwartz, T., Hutchison, J. A., Genet, C. & Ebbesen, T. W. Reversible switching of ultrastrong light-molecule coupling. *Phys. Rev. Lett.* **106**, 196405, DOI: 10.1103/PhysRevLett.106.196405 (2011).

25. Niemczyk, T. *et al.* Circuit quantum electrodynamics in the ultrastrong-coupling regime. *Nat. Phys.* **6**, 772–776, DOI: 10.1038/nphys1730 (2010).

26. Jouy, P. *et al.* Transition from strong to ultrastrong coupling regime in mid-infrared metal-dielectric-metal cavities. *Appl. Phys. Lett.* **98**, 231114, DOI: 10.1063/1.3598432 (2011).

27. George, J. *et al.* Multiple rabi splittings under ultrastrong vibrational coupling. *Phys. Rev. Lett.* **117**, 153601, DOI: 10.1103/PhysRevLett.117.153601 (2016).

28. Scalari, G. *et al.* Ultrastrong coupling of the cyclotron transition of a 2d electron gas to a thz metamaterial. *Science* **335**, 1323–1326, DOI: 10.1126/science.1216022 (2012).

29. Shelton, D. J. *et al.* Strong coupling between nanoscale metamaterials and phonons. *Nano Lett.* **11**, 2104–2108, DOI: 10.1021/nl200689z (2011).

30. Autore, M. *et al.* Boron nitride nanoresonators for phonon-enhanced molecular vibrational spectroscopy at the strong coupling limit. *Light. Sci. Appl.* **7**, 17172, DOI: 10.1038/lsa.2017.172 (2018).

31. Lather, J., Bhatt, P., Thomas, A., Ebbesen, T. W. & George, J. Cavity catalysis by cooperative vibrational strong coupling of reactant and solvent molecules. *Angew. Chem. Int. Ed.* **58**, 10635–10638, DOI: 10.1002/anie.201905407 (2019).

32. Jin, X. *et al.* Reshaping the phonon energy landscape of nanocrystals inside a terahertz plasmonic nanocavity. *Nat. Commun.* **9**, 763, DOI: 10.1038/s41467-018-03120-3 (2018).

33. Muller, E. A. *et al.* Nanoimaging and control of molecular vibrations through electromagnetically induced scattering reaching the strong coupling regime. *ACS Photonics* **5**, 3594–3600, DOI: 10.1021/acsphotonics.8b00425 (2018).

34. Baida, F. I., Belkhir, A., Labeke, D. V. & Lamrous, O. Subwavelength metallic coaxial waveguides in the optical range: Role of the plasmonic modes. *Phys. Rev. B* **74**, 205419, DOI: 10.1103/PhysRevB.74.205419 (2006).

35. Alù, A. & Engheta, N. Light squeezing through arbitrarily shaped plasmonic channels and sharp bends. *Phys. Rev. B* **78**, 035440, DOI: 10.1103/PhysRevB.78.035440 (2008).

36. Yoo, D. *et al.* High-throughput fabrication of resonant metamaterials with ultrasmall coaxial apertures via atomic layer lithography. *Nano Lett* **16**, 2040–2046, DOI: 10.1021/acs.nanolett.6b00024 (2016).

37. Liberal, I. & Engheta, N. Near-zero refractive index photonics. *Nat. Photonics* **11**, 149–158, DOI: 10.1038/nphoton.2017.13 (2017).

38. Garcia-Vidal, F. J., Martin-Moreno, L., Ebbesen, T. W. & Kuipers, L. Light passing through subwavelength apertures. *Rev. Mod. Phys.* **82**, 729–787, DOI: 10.1103/RevModPhys.82.729 (2010).

39. Kischkat, J. *et al.* Mid-infrared optical properties of thin films of aluminum oxide, titanium dioxide, silicon dioxide, aluminum nitride, and silicon nitride. *Appl. Opt.* **51**, 6789–6898, DOI: 10.1364/AO.51.006789 (2012).

40. Born, M. & Huang, K. *Dynamical Theory of Crystal Lattices* (Oxford University Press, 1988).

41. Hopfield, J. J. Theory of the contribution of excitons to the complex dielectric constant of crystals. *Phys. Rev.* **112**, 1555–1567, DOI: 10.1103/PhysRev.112.1555 (1958).

42. Quattropani, A., Andreani, L. C. & Bassani, F. Quantum theory of polaritons with spatial dispersion: Exact solutions. *Il Nuovo Cimento D* **7**, 55–69, DOI: 10.1007/BF02452395 (1986).

43. Ciuti, C., Bastard, G. & Carusotto, I. Quantum vacuum properties of the intersubband cavity polariton field. *Phys. Rev. B* **72**, 115303, DOI: 10.1103/PhysRevB.72.115303 (2005).

44. Todorov, Y. & Sirtori, C. Intersubband polaritons in the electrical dipole gauge. *Phys. Rev. B* **85**, 045304, DOI: 10.1103/PhysRevB.85.045304 (2012).

45. Kéna-Cohen, S., Maier, S. A. & Bradley, D. D. C. Ultrastrongly coupled exciton–polaritons in metal-clad organic semiconductor microcavities. *Adv. Opt. Mater.* **1**, 827–833, DOI: 10.1002/adom.201300256 (2013).

46. Cirio, M., De Liberato, S., Lambert, N. & Nori, F. Ground state electroluminescence. *Phys. Rev. Lett.* **116**, 113601, DOI: 10.1103/PhysRevLett.116.113601 (2016).

47. Kockum, A. F., Miranowicz, A., Macrì, V., Savasta, S. & Nori, F. Deterministic quantum nonlinear optics with single atoms and virtual photons. *Phys. Rev. A* **95**, 063849, DOI: 10.1103/PhysRevA.95.063849 (2017).

48. Garziano, L. *et al.* One photon can simultaneously excite two or more atoms. *Phys. Rev. Lett.* **117**, 043601, DOI: 10.1103/PhysRevLett.117.043601 (2016).

49. Kockum, A. F., Macrì, V., Garziano, L., Savasta, S. & Nori, F. Frequency conversion in ultrastrong cavity qed. *Sci. Rep.* **7**, 5313, DOI: 10.1038/s41598-017-04225-3 (2017).

Acknowledgements

Author contributions statement

D.Y. performed device design, fabrication, and measurements. F.dL.P. and L.M.M. developed theories and performed numerical calculations. D.A.M. and I.-H.L. performed computer simulations. M.P., M.B.R., and J.D.C. analyzed the results. All authors analyzed the data and wrote the paper together.

Additional information

Competing interests: The authors declare no competing interests
Data availability: The data that support the plots within this paper and other findings of this study are available from the corresponding author upon reasonable request.